



Contents lists available at ScienceDirect

## Materials and Design

journal homepage: [www.elsevier.com/locate/matdes](http://www.elsevier.com/locate/matdes)

## Bio-inspired armor protective material systems for ballistic shock mitigation

Jinhua Huang <sup>a,\*</sup>, Helen Durden <sup>a</sup>, Mostafiz Chowdhury <sup>b</sup><sup>a</sup> M4 Engineering, Inc., 4020 Long Beach Blvd., Long Beach, CA 90807, USA<sup>b</sup> Army Research Laboratory Liaison, 2511 Jefferson Davis Hwy., Arlington, VA 22202, USA

## ARTICLE INFO

## Article history:

Received 29 January 2011

Accepted 25 March 2011

Available online xxxx

## Keywords:

B. Foams

E. Impact and ballistic

G. Coupon testing

## ABSTRACT

Severe transient ballistic shocks from projectile impacts, mine blasts, or overhead artillery attacks can incapacitate an occupant at low frequencies, or sensitive equipment at high frequencies, if they are not properly attenuated by armor protective systems. Unique challenges exist in developing armor protective systems for mitigating both low and high frequency ballistic shocks due to the lack of robust design methodology, the severe dynamic loading conditions, and the uncertainties in predicting ballistic shock responses.

Nature offers engineers a blueprint of highly effective, efficient, and adaptive material designs to protect certain regions from external threats. This paper presents the modeling, analysis, design, optimization, fabrication, and experimental validation of bone-inspired armor protective material systems for reducing projectile penetrations and alleviating ballistic shocks at both low and high frequencies. The optimized bone-inspired armor protective material system has a soft-stiff-soft-stiff material distribution pattern based on bone-foramen and osteonal-bone material systems. Analysis and experimental results demonstrated that the bone-inspired armor protective material systems have excellent capabilities for drastic ballistic shock mitigation, weight savings, and significant reductions in penetration and load transmission under ballistic loading conditions.

© 2011 Elsevier Ltd. All rights reserved.

## 1. Introduction

The necessity of considering ballistic shock effects in new vehicle designs has been well recognized in the combat vehicle community during the past two decades [1]. A ballistic shock results from a significant amount of concentrated energy deposited from caliber projectile impacts, mine blasts, or overhead artillery attacks onto a small area of a military vehicle [2]. This energy may be transmitted throughout the vehicle including areas far away from and not exposed to the incident agent. At low frequencies (up to 1 kHz), the ballistic shock response is dominated by high load transmissions and large-magnitude flexural vibrations, which can be fatal to humans in a demanding high-g environment. A shock of 100 g for 3 ms or 40 g for 50 ms will cause severe injury [3]. At high frequencies (above 1 kHz), the ballistic shock response is dominated by the propagation of the stress waves in the vehicle materials, which will damage the light, intricate, frequency-sensitive components such as electronics and optics. Despite the recognized increasing demand for innovative lightweight armor protective systems capable of mitigating both low and high frequency ballistic shocks, the development of the enabling techniques to support such armor protective system analysis and design has been slow.

This is due to the severe dynamic loading conditions, the uncertainties in predicting ballistic shock responses, the difficulty in selecting proper constituent materials, and difficulties in determining critical material and geometry design variables.

In ballistic shock analysis, finite element based commercial software, especially LS-Dyna, has been predominately utilized to calculate the target shock responses including acceleration histories, shock response spectra, deformation, penetration, velocities, and severity indices [4–6]. Due to the high frequency range of ballistic shock, the finite element based methods can become intractable for large structures. A statistical energy analysis (SEA) method was investigated for the prediction of ballistic shock in combat vehicles [1]. Compared to conventional analysis methods, the SEA method results in faster model construction, smaller model sizes, shorter running time, and a reduced set of input parameters. However, the SEA predictions at some locations within the test component might disagree significantly from the experimental measurements [1].

Many efforts have been made to mitigate ballistic shocks. Trabia et al., employed side and bottom L-shape panel joints for a combat vehicle to mitigate ballistic shocks from projectile and blast attacks [5,6]. The optimization results showed that the average of the mean of accelerations at critical locations in commander and driver seats and instrumentation panels could be reduced considerably by extending the joint and reducing its thickness. One drawback of the panel joint approach is its strong dependence on applied

\* Corresponding author. Tel.: +1 562 981 7797; fax: +1 562 490 8568.

E-mail address: [jhuang@m4-engineering.com](mailto:jhuang@m4-engineering.com) (J. Huang).

Report Documentation Page			Form Approved OMB No. 0704-0188	
<p>Public reporting burden for the collection of information is estimated to average 1 hour per response, including the time for reviewing instructions, searching existing data sources, gathering and maintaining the data needed, and completing and reviewing the collection of information. Send comments regarding this burden estimate or any other aspect of this collection of information, including suggestions for reducing this burden, to Washington Headquarters Services, Directorate for Information Operations and Reports, 1215 Jefferson Davis Highway, Suite 1204, Arlington VA 22202-4302. Respondents should be aware that notwithstanding any other provision of law, no person shall be subject to a penalty for failing to comply with a collection of information if it does not display a currently valid OMB control number.</p>				
1. REPORT DATE <b>JAN 2011</b>	2. REPORT TYPE	3. DATES COVERED <b>00-00-2011 to 00-00-2011</b>		
4. TITLE AND SUBTITLE <b>Bio-inspired armor protective material systems for ballistic shock mitigation</b>			5a. CONTRACT NUMBER	
			5b. GRANT NUMBER	
			5c. PROGRAM ELEMENT NUMBER	
6. AUTHOR(S)			5d. PROJECT NUMBER	
			5e. TASK NUMBER	
			5f. WORK UNIT NUMBER	
7. PERFORMING ORGANIZATION NAME(S) AND ADDRESS(ES) <b>Army Research Laboratory Liaison, 2511 Jefferson Davis Hwy, Arlington, VA, 22202</b>			8. PERFORMING ORGANIZATION REPORT NUMBER	
9. SPONSORING/MONITORING AGENCY NAME(S) AND ADDRESS(ES)			10. SPONSOR/MONITOR'S ACRONYM(S)	
			11. SPONSOR/MONITOR'S REPORT NUMBER(S)	
12. DISTRIBUTION/AVAILABILITY STATEMENT <b>Approved for public release; distribution unlimited</b>				
13. SUPPLEMENTARY NOTES				
14. ABSTRACT <p><b>Severe transient ballistic shocks from projectile impacts, mine blasts, or overhead artillery attacks can incapacitate an occupant at low frequencies, or sensitive equipment at high frequencies, if they are not properly attenuated by armor protective systems. Unique challenges exist in developing armor protective systems for mitigating both low and high frequency ballistic shocks due to the lack of robust design methodology, the severe dynamic loading conditions, and the uncertainties in predicting ballistic shock responses. Nature offers engineers a blueprint of highly effective, efficient, and adaptive material designs to protect certain regions from external threats. This paper presents the modeling, analysis, design, optimization fabrication, and experimental validation of bone-inspired armor protective material systems for reducing projectile penetrations and alleviating ballistic shocks at both low and high frequencies. The optimized bone-inspired armor protective material system has a soft?stiff?soft?stiff material distribution pattern based on bone-foramen and osteonal-bone material systems. Analysis and experimental results demonstrated that the bone-inspired armor protective material systems have excellent capabilities for drastic ballistic shock mitigation, weight savings, and significant reductions in penetration and load transmission under ballistic loading conditions.</b></p>				
15. SUBJECT TERMS				
16. SECURITY CLASSIFICATION OF:			17. LIMITATION OF ABSTRACT <b>Same as Report (SAR)</b>	18. NUMBER OF PAGES <b>9</b>
a. REPORT <b>unclassified</b>	b. ABSTRACT <b>unclassified</b>	c. THIS PAGE <b>unclassified</b>	19a. NAME OF RESPONSIBLE PERSON	

load locations. Doney and Sen studied the shock mitigation efficiency of metallic tapered chains (highly scalable granular media) [7]. While the metallic tapered chain armor demonstrates noticeable shock absorption, it lacks good penetration-resistance capability, its heavy weight scarifies the vehicle's mobility, and its fabrication is not cheap. Polymer-matrix composite (PMC) based armor was developed to improve the ballistic performance of rapidly deployable lightweight vehicles [8]. However, revolutionary improvements in PMC-based armor designs are required to reach Army myriad performance goals for ballistic, structural, shock, fire, cost, and signature. Dharmasena et al., investigated the dynamic mechanical response of square honeycomb panels made from a super-austenitic stainless steel alloy [9]. The benefits of the square honeycomb panels for blast mitigation are particularly evident at low impulsive levels, but at high impulse levels, the benefits diminish.

Through millions of years of evolution to solve load-bearing problems and adapt to a given environment, nature offers engineers a blueprint of highly effective, efficient, and adaptive material designs to protect certain regions from external threats [10–12]. The bone-foramen material system in a region of a horse's third metacarpus (Fig. 1), which is located in the forelimb of the horse, consists of a foramen (natural hole) and foam materials, and is subject to impact loading. The normal horse third metacarpus is osteonal-bone that is composed of interstitial (lamellae), cement line, and osteons (Haversian systems) (Fig. 2). Both bone-foramen and osteonal-bone material systems have developed very robust design patterns to protect blood vessels and nerves. Experimental measurements on bone-foramen and osteonal-bone material systems have revealed stiffness distribution patterns due to functionally graded density variations [12,13]. The bone-foramen material system has a soft region near the foramen and a stiffer region some distance away, compared with normal bone properties (far field). The modulus in the osteonal-bone material system has a relatively high value in the interstitial matrix field and gradually becomes smaller in the cement line. It reaches a high value again in the intra-osteon region.

Great parallels exist between the horse's third metacarpus and engineering armor protective systems in material constituents, loading conditions, design goals, design constraints, and design methodology [12]. This led us to a US Army sponsored effort to develop an innovative, lightweight bone-inspired functionally graded armor protective material system for ballistic shock mitigation and penetration reduction. The current paper presents the research results for the bone-inspired armor project. In what follows, we first describe the concept formulation of bone-inspired armor protective material systems. Next, we present the analysis and optimization of bone-inspired armor protective material systems. Then, the enhancement of the optimized bone-inspired armor protective material system is discussed. Experimental validation is given in Section 5. Finally, we draw conclusions in Section 6.

## 2. Concept formulation of bone-inspired armor protective material systems

### 2.1. Natural bone protection material systems

The bone-foramen (Fig. 1) and osteonal-bone (Fig. 2) protective systems of the equine third metacarpus (MC3) consist of foam materials. The homogenized elastic modulus ( $E_{bone}$ ) and strength ( $\sigma_{bone}$ ) of these foam materials increase with the bone apparent density ( $\rho_{bone}$ ) and can be expressed by the following power law functions [12–14]:

$$E_{bone} = a\rho_{bone}^b \quad (1)$$

$$\sigma_{bone} = \alpha\rho_{bone}^\beta \quad (2)$$

where  $a$ ,  $\alpha$ ,  $b$ , and  $\beta$  are constants and  $b/\beta = 0.5$  for osteonal bones. Experimental measurements and property correlations for the bone-foramen and osteonal-bone material systems revealed the following important features [12,13,15]:

- The material density and property are spatially graded.
- There exist stiff, strong regions and soft, weak regions.
- There is no discontinuity in density or property distributions at the juncture between different regions.
- Material property variations are limited to regions around the foramen and within the cement line and intra-osteon.
- There exist special fiber orientation distribution patterns in certain regions as opposed to normal fiber orientations.
- Osteonal-bone has an effective crack-stopping mechanism [15].

### 2.2. Parallels between bone and engineering designs

In both bone-foramen and osteonal-bone material systems, the designs are achieved through mechanical property gradation under weight constraints and impact loading conditions and the designs aim to protect internal regions from external threats. In the vehicle armor protective system design, the weight is also constrained due to mobility requirement and the design also aims to protect internal regions from external threats due to projectile impacts and mine blasts. The design spaces for both bone and vehicle armor protective systems are very limited.

Similar to the utilization of foams in bone-foramen and osteonal-bone protective system designs, metallic foams have found applications in vehicle armor designs [16,17]. For both bone and metallic foams, the material properties (modulus, strength, Poisson's ratio, etc.) depend on density. The bone-foramen and osteonal-bone material systems optimize mechanical property gradations by spatially varying the bone foam material's void and solid phase distributions. Similarly, the spaced vehicle armor design utilizes the spatial void (spaces between plates) and solid

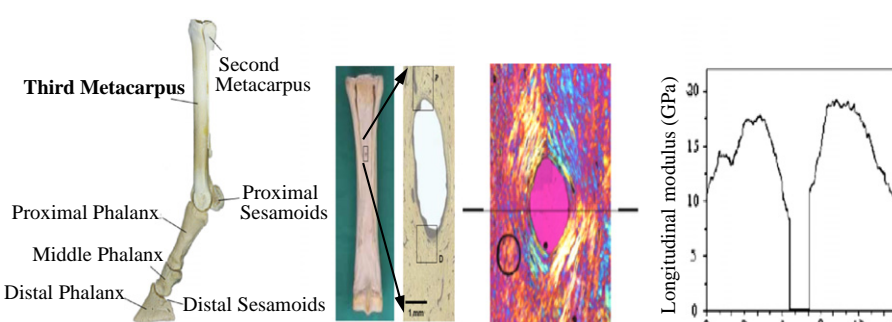


**Fig. 1.** Horse forelimb bones (left), third metacarpus palmar and photomicrograph of the foramen (middle), and modulus distribution along foramen mediolateral line (right).

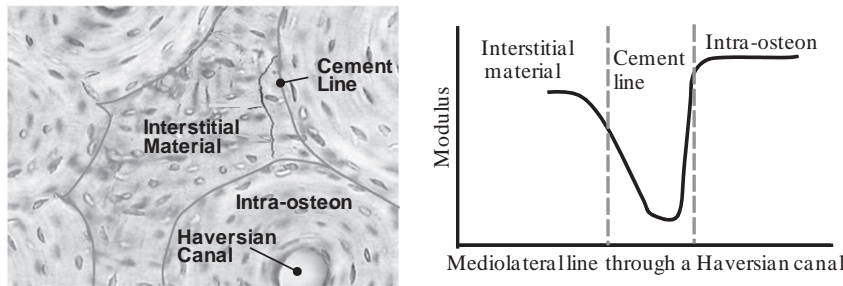


**Fig. 2.** Features of typical osteonal-bone (left) and modulus variation through an osteon.

(plates) phase distributions. Compared to spaced armor designs, the bone-foramen and osteonal-bone designs have functionally graded void and solid phase distribution, which is more effective in strengthening the protection capability.

### 2.3. Bone-inspired armor protective material systems

Design of vehicle armor is based on plate panels. Spaced, flat, sloped, or other armor designs are constructed using these panels. Therefore, a flat plate geometry with a specified thickness was considered for bone-inspired armor protective material systems for ballistic shock mitigation. In accordance with the parallels between bone and engineering designs, a bone-inspired armor protective system was constructed using functionally graded foam materials. The bone-inspired armor plate was divided along its thickness direction into a near field ( $\Omega_n$ ) in the protection side and a far field ( $\Omega_f$ ) in the external loading side as shown in Fig. 3. The far field has constant density and material properties. The density and material properties vary continuously in the near field and smoothly bridge into the far field.

As the mechanical properties of a foam material depend on its density, the bone-inspired armor design problem becomes: determine the through-thickness far and near field foam density distribution curves so that the ballistic shock response can be mitigated. The curve for maximum ballistic shock mitigation is achieved through an optimization method. During the optimization process, any density distribution curve could be generated. The following Bezier functions were employed to represent arbitrary density distribution curves:

$$\begin{cases} t_i = \frac{i}{10}t_{near} & (i = 0, 1, \dots, 10) \\ t = \sum_{i=0}^{10} \binom{10}{i} t_i s^i (1-s)^{10-i} & (0 \leq s \leq 1, 0 \leq t \leq t_{near}) \\ \rho_{min} \leq \rho = \sum_{i=0}^8 \binom{10}{i} \rho_i s^i (1-s)^{10-i} + \rho_{far} s^9 (10 - 9s) \leq \rho_{max} & (0 \leq s \leq 1, 0 \leq t \leq t_{near}) \\ \rho_{min} \leq \rho = \rho_{far} \leq \rho_{max} & (t_{near} \leq t \leq t_{near} + t_{far}) \end{cases} \quad (3)$$

where  $\binom{10}{i} = \frac{10!}{i!(10-i)!}$ ,  $s$  is the normalized thickness coordinate,  $\rho$  is the density at coordinate  $s$ ,  $t_{near}$  is the near field width,  $t_{far}$  is the far

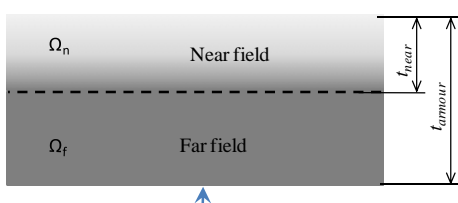


**Fig. 3.** Near and far fields for a bone-inspired armor protective material system. The arrow represents load location and direction.

field width,  $\rho_{min}$  is the minimum allowed density,  $\rho_{max}$  is the maximum allowed density,  $\rho_{far}$  is the far field density,  $\rho_i$  ( $i = 0, \dots, 10$ ) are the foam density controllers, and  $t_i$  ( $i = 0, \dots, 10$ ) are the locations for the foam density controllers. When  $\rho_9$  and  $\rho_{10}$  are set equal to  $\rho_{far}$ , the above functions satisfy  $C^\infty$  continuity in the near and far fields and  $C^1$  continuity at the near and far field intersection. When the values of the density controllers are varied, the Bezier curve is updated accordingly.

### 2.4. Material description

A number of metallic foams are suitable for the design of the bone-inspired armor protective material system. In this paper, aluminum foam from Alulight America was selected and modeled/analyzed as typical honeycomb orthotropic crush material [18]. In the honeycomb crush model, the material behavior is composed of three phases: linear elastic loading with modulus  $E_e$ , volumetric crush to strain  $\varepsilon_c$  at constant crush stress  $\sigma_y$ , and hardening to full compaction with modulus  $E_c$ . The parameters  $E_e$ ,  $\varepsilon_c$ , and  $\sigma_y$  are expressed as explicit functions of density based on closed-cell metallic foams [16] and material property data provided by Alulight:

$$E_e = 69 \left( \frac{\rho}{\rho_s} \right)^{1.6} \text{ (GPa)} \quad (4)$$

$$\sigma_y = 43.89 \left[ 0.5 \left( \frac{\rho}{\rho_s} \right)^{2/3} + 0.3 \left( \frac{\rho}{\rho_s} \right) \right] \text{ (MPa)} \quad (5)$$

$$\varepsilon_c = 0.95 \left[ 1 - 1.4 \frac{\rho}{\rho_s} + 0.4 \left( \frac{\rho}{\rho_s} \right)^3 \right] \quad (6)$$

where  $\rho$  is the density and  $\rho_s$  is the density of the solid cell wall.

To take into account the strain rate effect, a stress enhancement coefficient of 1.5 times the static stress was used to model the crushing stress on the Alulight aluminum foam material [18].

### 3. Analysis and optimization

A gas gun test scenario was simulated for the evaluation of the bone-inspired protective material system by utilizing a rectangular coupon. In this scenario, the coupon was held with a steel support with a central hole for measurement access, and a high-speed cylindrical projectile was shot towards the coupon front face (Fig. 4). The coupon is represented by its cross section edge length, near and far field widths, as well as the far field density,  $\rho_{far}$  and the near field density controllers  $\rho_0$  through  $\rho_{10}$  with  $\rho_9 = \rho_{10} = \rho_{far}$  for continuity consideration. The coupon acceleration history at the back face in the penetration direction was simulated using LS-Dyna. All simulations were terminated at a time of 15 ms. The corresponding shock response spectrum was obtained through a MATLAB program based on Kelly–Richman algorithm [19].

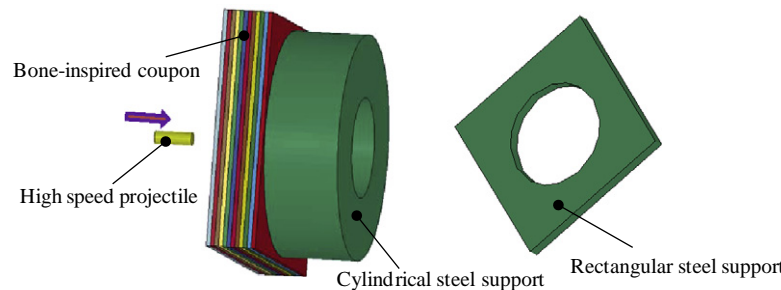


**Fig. 4.** Models for bone-inspired design simulation under high-speed projectile loading conditions.

To compare the shock mitigation performance of bone-inspired coupons, baseline analyses with uniform Alulight aluminum foam densities of  $350 \text{ kg/m}^3$ ,  $419 \text{ kg/m}^3$ ,  $650 \text{ kg/m}^3$ ,  $710 \text{ kg/m}^3$ ,  $980 \text{ kg/m}^3$ , and  $1370 \text{ kg/m}^3$  were performed. The maximum acceleration vs. density curve and the shock response spectra for these uniform foams are displayed in Figs. 5 and 6.

For the bone-inspired coupon optimization, the maximum acceleration ( $ma_{\text{Acc}}$ ) at the coupon protection point (back face center) was selected as the objective function. The design variables are the far field density,  $\rho_{\text{far}}$  and the near field density controllers  $\rho_0$  through  $\rho_8$ . The near field density controllers  $\rho_9$  and  $\rho_{10}$  were set equal to  $\rho_{\text{far}}$  to satisfy  $C^1$  density distribution continuity requirement at the near and far field intersection. The overall average density  $\rho_{\text{average}} \leq 710 \text{ kg/m}^3$  constraint was used for weight-based vehicle mobility considerations and all densities were constrained by the available material range except a narrow band near the protection side where the densities were allowed to reach the value of the solid cell wall. The optimization problem was found to have many local optima due to numerical noise. To find a relatively robust solution, a gradient-based optimization method was employed with multiple initial points. The best points are reported in this paper. The optimum through-thickness density distribution curve is presented in Fig. 7. The corresponding acceleration magnitude history and shock response spectrum results are separately plotted in Figs. 8 and 9. A summary is shown in Table 1.

For uniform density coupons, the maximum acceleration changes only slightly when the density is increased (Fig. 5). In some cases, a relative density increase gives rise to an increase in

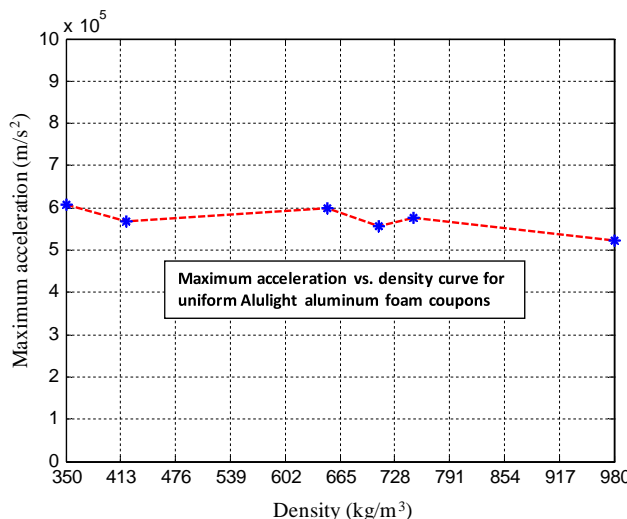


**Fig. 5.** Simulated maximum acceleration vs. density curve for uniform density aluminum foam coupons.

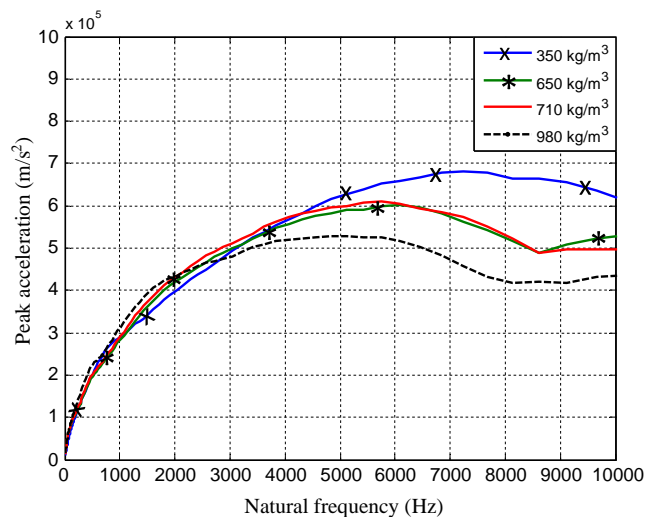


**Fig. 6.** Simulated shock response spectra for uniform Alulight aluminum foam coupons at the densities of  $350 \text{ kg/m}^3$ ,  $650 \text{ kg/m}^3$ ,  $710 \text{ kg/m}^3$ , and  $980 \text{ kg/m}^3$ .

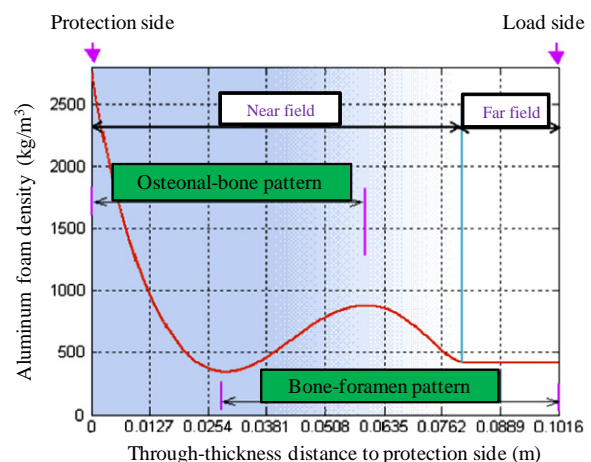


**Fig. 7.** Optimized bone-inspired through-thickness foam density distribution under the weight constraint of  $\rho_{\text{average}} \leq 710 \text{ kg/m}^3$ .

the maximum acceleration. In the shock response spectra, increasing the density increases the peak acceleration at low frequencies up to 2800 Hz (Fig. 6). Such low frequency reactions can be fatal to humans. There is no single uniform density aluminum foam coupon that can both decrease the maximum acceleration and the low frequency peak accelerations from the shock response spectra.

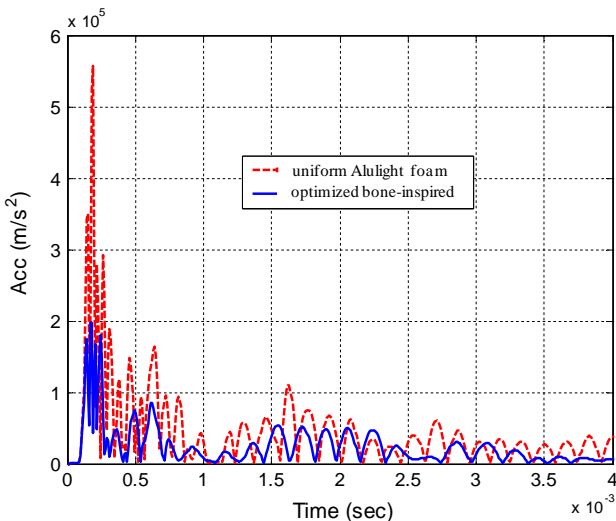


**Fig. 8.** Simulated acceleration magnitude histories for the  $\rho_{\text{average}} \leq 710 \text{ kg/m}^3$  constrained optimized bone-inspired design and for the uniform design of the same weight ( $\rho = 708 \text{ kg/m}^3$ ).

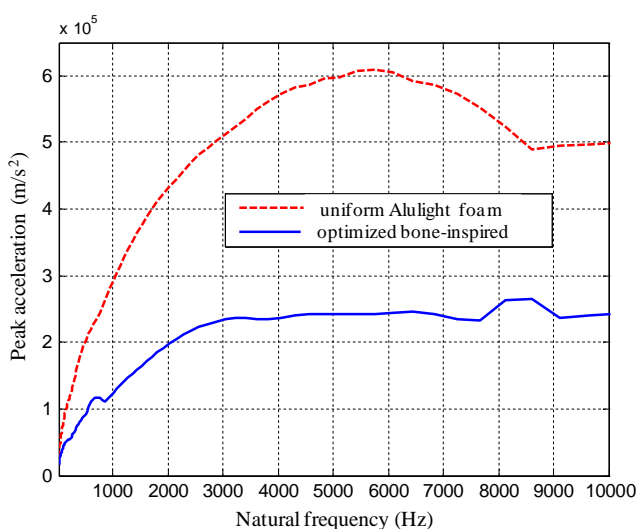


**Fig. 9.** Simulated shock response spectra for the  $\rho_{\text{average}} \leq 710 \text{ kg/m}^3$  constrained optimized bone-inspired design and for the uniform design of the same weight ( $\rho = 708 \text{ kg/m}^3$ ).

The optimized bone-inspired designs show features from both bone-foramen and osteonal-bone material systems (Fig. 7). The optimized designs between the far field and the soft region (the lowest density point in Fig. 7) in the near field utilize the bone-foramen material design mechanism. Between the two stiff regions (the two relatively high density points in Fig. 7), the optimized

**Table 1**

Simulated maximum accelerations and average densities for the optimized bone-inspired design in comparison with the results of the uniform design of the same weight.

Designs	Maximum acceleration (m/s <sup>2</sup> )	Average density (kg/m <sup>3</sup> )
Optimized bone-inspired, $\rho_{\text{average}} \leq 710 \text{ kg/m}^3$	$1.97 \times 10^5$	708
Uniform design with $\rho = 708 \text{ kg/m}^3$	$5.6 \times 10^5$	708

designs utilize the osteonal-bone material design mechanism. There is a narrow band in the stiff region near the protection side where the density varies from  $1370 \text{ kg/m}^3$  to the value of the solid cell wall. This high density band can be produced by pre-compressing low density aluminum foams or can be replaced by solid materials.

The maximum acceleration for the optimized bone-inspired design is only a small fraction of the corresponding maximum acceleration of the uniform foam design of the same weight (Table 1 and Fig. 8). More importantly, the optimized bone-inspired design can dramatically reduce the peak accelerations at both low and high frequencies (Fig. 9). The optimization results demonstrated that minimizing the maximum acceleration minimizes the peak accelerations over all frequencies in the shock response spectra.

Due to the high numerical noise in the finite element-based analyses, the solution from the gradient-based method might be still local optima. With a more robust optimization algorithm such as a combined genetic and gradient method [12], the ballistic shock response is expected to be further mitigated at a relatively small average density constraint.

#### 4. Enhancement of optimized design

As shown in Fig. 7, the optimized foam density distribution shows a very dense, stiff layer on the protection side. Thin steel plates replacing the protection side dense layer were investigated as enhancements to the optimized design. The enhanced optimized bone-inspired design has an average density of  $1275 \text{ kg/m}^3$ . The acceleration magnitude histories and the shock response spectra for the enhanced, the optimized, and the uniform density designs of the same weight are shown in Figs. 10 and 11.

The inclusion of a thin stiff metallic (steel) plate into the optimized bone-inspired design has a particularly effective response for ballistic shock mitigation, with the maximum acceleration reduced by nearly a factor of ten from the uniform foam coupon of the same weight (Fig. 10) and the peak accelerations in the shock response spectra reduced to very low levels in the frequency range between 10 Hz and 10,000 Hz (Fig. 11).

#### 5. Experimental validation

##### 5.1. Coupon gas gun validation tests

In the gas gun validation tests, both uniform density and bone-inspired coupons were subjected to the loading of a cylindrical hard steel projectile shot from a gas gun around a given velocity. To reduce the fabrication cost, the bone-inspired coupons were designed through trade-studies using discrete layers and a small number of aluminum foam densities to approximate the material distribution pattern shown in Fig. 7. A thin steel plate was bonded to the protection side to enhance the shock mitigation capability of the bone-inspired designs. The uniform density coupons have the same dimensions as the bone-inspired design models. For all gas gun tests, the acceleration history in the penetration direction at a back face point (protection side) was recorded using an accelerometer.

##### 5.1.1. Gas gun test setup

The gas gun test configuration consists of a gas gun, a steel projectile, and a coupon clamped between a front face constraint and a back face support as shown in Fig. 12. Both the front face constraint and back face support were made of rectangular steel plates and have dimensions of  $139.7 \text{ mm} \times 139.7 \text{ mm} \times 9.65 \text{ mm}$  with a central hole of  $85.7 \text{ mm}$  diameter. The steel projectile has a diameter

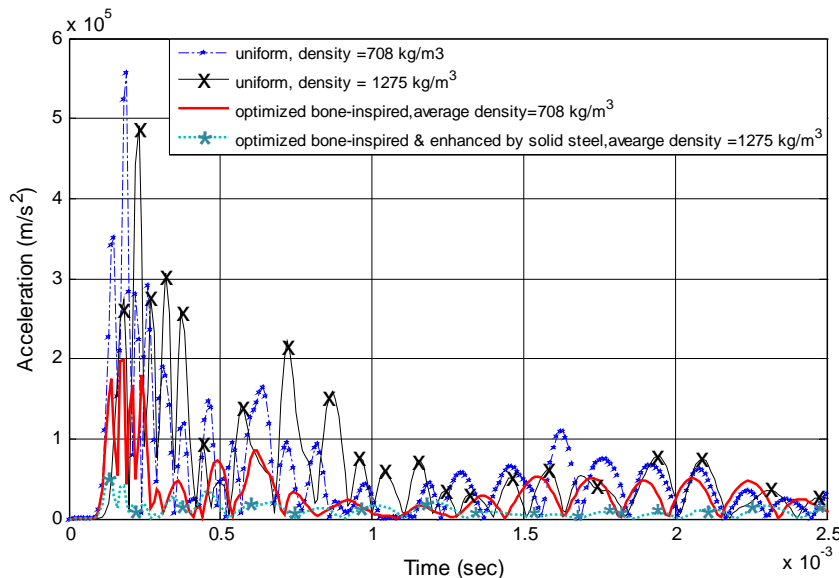


**Fig. 10.** Simulated acceleration magnitude histories with respect to the optimized bone-inspired design, enhanced optimized design with a thin steel plate, and  $708 \text{ kg/m}^3$  and  $1275 \text{ kg/m}^3$  uniform density designs.

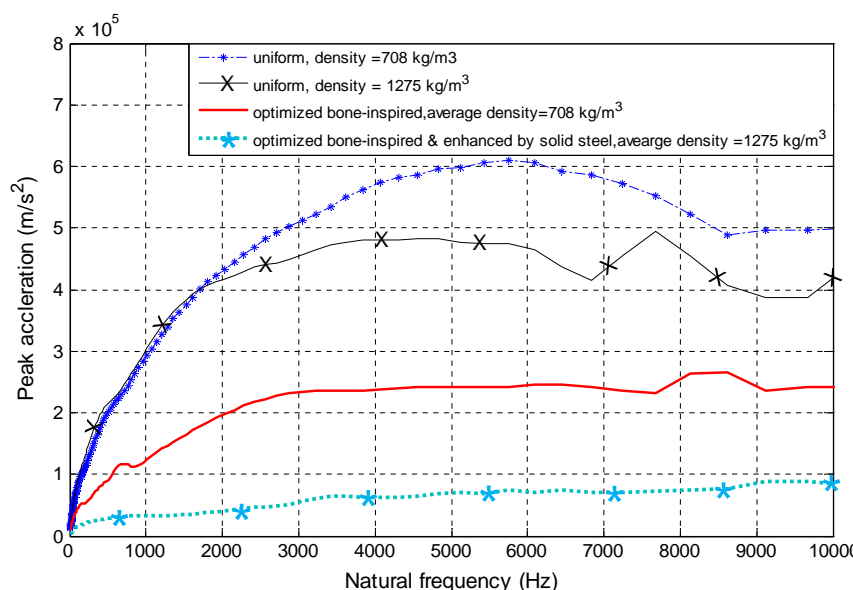


**Fig. 11.** Simulated shock response spectra with respect to the optimized bone-inspired design, enhanced optimized design with a thin steel plate, and  $708 \text{ kg/m}^3$  and  $1275 \text{ kg/m}^3$  uniform density designs.

of 12.7 mm and a height of 38.1 mm. The shooting velocity was designed to be 200 m/s.

#### 5.1.2. Coupon design under gas gun test conditions

The optimized bone-inspired coupon has demonstrated a special soft-stiff-soft-stiff material distribution (Fig. 7). This material distribution pattern was utilized to design the bone-inspired test coupons using discrete layers and a small number of foam densities. The coupon was divided into five regions along the thickness direction: Soft 1, Stiff 1, Soft 2, Stiff 2, and thin Steel plate as shown in Fig. 13. Based on trade-studies and the available densities from the Alulight warehouse, the five regional densities for good shock mitigation were determined as shown in Fig. 13. The average density for this enhanced bone-inspired design is about  $1320 \text{ kg/m}^3$ .

#### 5.1.3. Coupon fabrication

Raw 25.4 mm-thick aluminum foam plates with densities in Fig. 13 were ordered from Alulight America, and cut into 101.6 mm  $\times$  101.6 mm size. The thin steel metal plate and the machined foam plates were assembled using adhesive materials. The uniform density aluminum foam coupons were fabricated using the same method.

The test coupons were classified into A, B, E, and S groups. Group S is a sample consisting of low and high densities and was used to adjust the electronic instrument and the projectile velocity. Group E is the enhanced bone-inspired coupon as shown in Fig. 13. Group A has a uniform density of  $520 \text{ kg/m}^3$  and Group B has a uniform density of  $770 \text{ kg/m}^3$ . Higher density uniform coupons were not tested due to lack of available material.

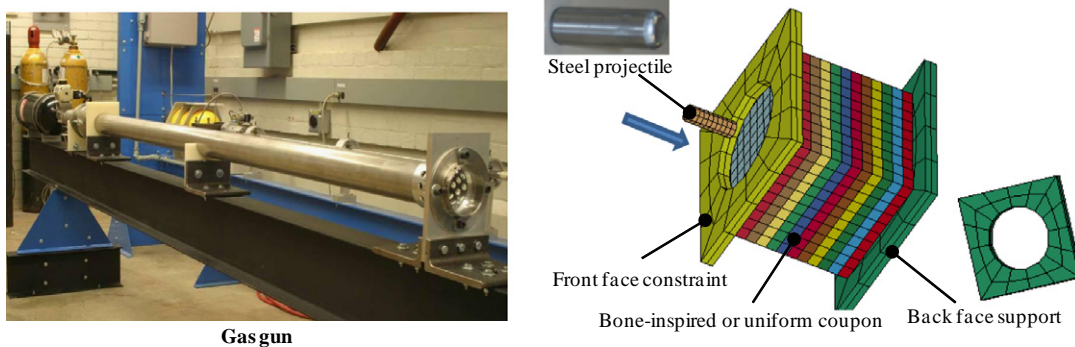


Fig. 12. Coupon gas gun test setup.

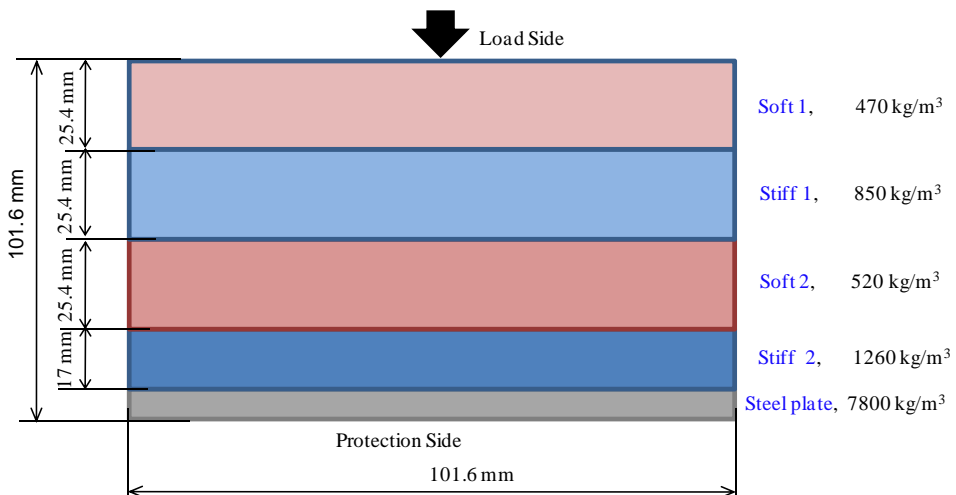


Fig. 13. Enhanced bone-inspired coupon thickness division into different regions and the corresponding densities.

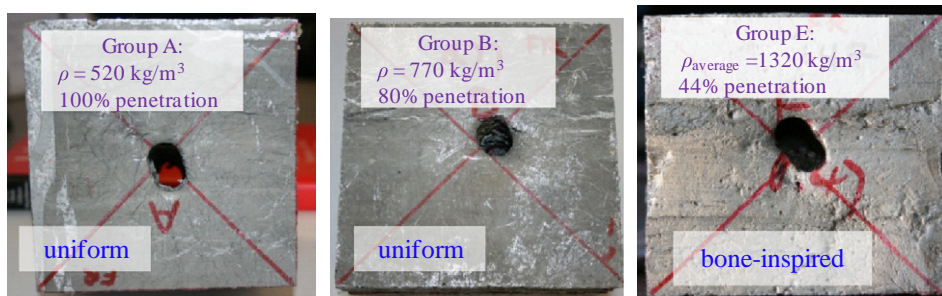


Fig. 14. Penetrations for both uniform and enhanced bone-inspired test coupons.

**Table 2**

Maximum accelerations for both uniform and enhanced bone-inspired coupons for the gas gun tests.

Group	A <sup>a</sup> (uniform)	B (uniform)	E (bone-inspired)		
			First central hit	Second central hit	3rd offset hit
Average density (kg/m <sup>3</sup> )	520	770	1320	1320	1320
Max acceleration (m/s <sup>2</sup> )	$3 \times 10^4$	$6 \times 10^4$	$1.1 \times 10^4$	$1.75 \times 10^4$	$2.3 \times 10^4$

<sup>a</sup> Complete penetration observed.

#### 5.1.4. Gas gun validation results

The test results include coupon penetrations, acceleration histories in the penetration directions, and material flow patterns. For

the enhanced bone-inspired coupon (Group E) test, a very small maximum acceleration was observed and recorded in the first central hit, but unfortunately the full acceleration history was

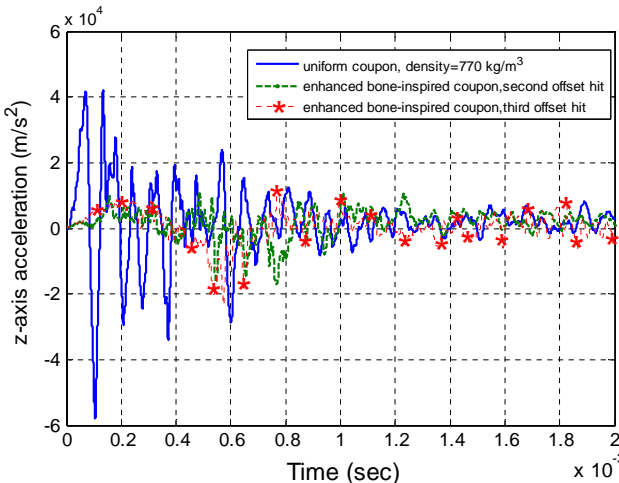


**Fig. 15.** Gas gun experimental acceleration histories in the penetration direction for the enhanced bone-inspired and the 770 kg/m<sup>3</sup> uniform density test coupons.

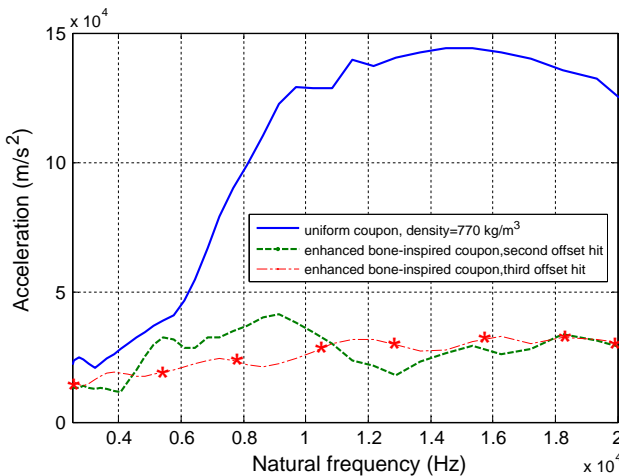


**Fig. 16.** Gas gun experimental shock response spectra for the enhanced bone-inspired and the 770 kg/m<sup>3</sup> uniform density test coupons.

not recorded. In a second attempt, the projectile went out from one lateral side. In the third attempt, the projectile had a 1–5% higher velocity and some rotation. The penetrations for Group A, B, and E (first central hit) are shown in Fig. 14. The measured maximum

accelerations are listed in Table 2. The measured acceleration histories in the penetration direction and the corresponding shock response spectra for Group B and E (second and third offset hits) are plotted in Figs. 15 and 16.

The projectile completely penetrated the 520 kg/m<sup>3</sup> low density uniform coupon and penetrated 80% of the 770 kg/m<sup>3</sup> high density uniform coupon (Fig. 14). The enhanced bone-inspired coupon proved very effective in reducing projectile penetration, to only 44% of the coupon thickness (Fig. 14).

The experimental results demonstrated that the maximum acceleration doubled when the uniform coupon density was increased from 520 kg/m<sup>3</sup> to 770 kg/m<sup>3</sup>. However, the actual maximum acceleration of the 520 kg/m<sup>3</sup> uniform density coupon might be higher than the recorded value due to the complete penetration. The measured maximum acceleration of the enhanced bone-inspired coupon is significantly lower than either uniform density coupon result (Table 2 and Fig. 15), which is consistent with the previous LS-Dyna analysis results (Fig. 10).

The experimental peak accelerations of the enhanced bone-inspired coupon in the corresponding shock response spectrum are greatly reduced over a wide range of frequencies compared to the 770 kg/m<sup>3</sup> uniform density coupon (Fig. 16).

To investigate the shock mitigation mechanism of bone-inspired armor protective material systems, two tested coupons were cut across the penetration hole. One was the 520 kg/m<sup>3</sup> uniform density coupon from Group A that had full penetration as shown in Fig. 17 (left). The other was the fully penetrated non-uniform sample coupon from Group S (Fig. 17 (right)) that was used to setup the facilities. The density distributions of this non-uniform sample coupon is shown in the same figure. Other coupons had only partial penetrations and were not cut as they contained hard steel projectile, but some observations could be made for visible portion. Based on the foam material flow patterns across the cut cross sections, the following important observations are obtained:

- For both uniform and non-uniform (including the bone-inspired) coupons, the material flows in both penetration and lateral directions.
- Uniform density coupons have a much more uniform penetration hole size (Fig. 17 (left)).
- For non-uniform coupons, the dense layers have relatively small penetration holes (Fig. 17 (right)).
- At the interface between low- and high-density layers, the foam has more lateral material flow, which contributes to the relaxation of the through-thickness shock and load transmissions.



**Fig. 17.** Through-thickness cross section cuts for the 520 kg/m<sup>3</sup> uniform density (Group A, left) and the non-uniform (Group S, right) test coupons.

## 6. Conclusions

The bone-inspired armor protective material systems have great potentials for reducing load transmission, weight savings, projectile penetration reduction, and shock mitigation at both low and high frequencies under high-speed projectile loading conditions. The optimized bone-inspired armor protective material system has a special soft-stiff-soft-stiff stiffness distribution. The performance of the optimized design can be significantly enhanced by an inclusion of a thin stiff metallic plate at the protection side. The enhanced optimized bone-inspired design can be approximated by using a limited number of discrete densities and a thin steel plate. Experimental results demonstrated that the performance of the enhanced approximated design (enhanced bone-inspired coupon using discrete densities and a thin steel plate) can match the enhanced optimized design (enhanced optimized bone-inspired design using functionally grade metallic foams and a thin steel plate).

The through-thickness density and material property distributions of bone-inspired armor protective material systems play a critical role in mitigating ballistic shocks and in reducing load transmissions and projectile penetrations. The stiff layers reflect the ballistic shock waves and change some of the shock wave transmission paths from the penetration direction to the lateral direction while the soft layers dissipating the kinetic energy through foam material crushing.

The enhanced bone-inspired coupons were designed and fabricated using a small number of aluminum foam densities due to time and budgetary constraints. With a generic optimized bone-inspired design, an integrated fabrication method, and comprehensive exploration of other metallic foam systems and thin stiff plate enhancements, greatly improved experimental results are expected for the bone-inspired material systems for ballistic shock mitigation and penetration reduction under user-specified weight constraint and various dynamic loading conditions.

## Acknowledgements

Research presented in this paper is funded through Army Research Laboratory via the M4 Engineering Inc., SBIR Contract W911QX-10-C-0043: Bone-Foramen-Inspired Material System for Ballistic Shock Mitigation.

## References

- [1] Loper B, Fryman A, Berman M, Li D. Validation of ballistic shock prediction models and techniques for use in the crusader combat vehicle program (U). 11th Annual US army ground vehicle survivability symposium; March 27–30, 2000.
- [2] Klopovic JT, Robinson WT, Petty DW, Sivack MR. An experimental, analysis, and model of ballistic shock. US Army Research Laboratory, ARL-MR-368; 1997.
- [3] Shmulevich I, Asaf Z. Going ballistic, vehicle ballistics protection and testing-defense. *Manage J* 1999;44.
- [4] Chowdhury MR, Bouland A. Ballistic shock FEM and parametric study of the FCS/SAC-11 vehicle. US Army Research Laboratory, ARL-TR-4331; 2007.
- [5] Trabia M, Huang J, O'Toole B, Sakaray U. Optimization of joint design for bottom panel of a military vehicle for shock reduction under blast loading. 77th Shock & vibration symposium, Monterey, CA; 2006.
- [6] Trabia M, O'Toole B, Ladkany S, Naraparaju J, Huang J. Optimization of joint design for side panel of a military vehicle for shock reduction. 76th Shock & vibration symposium, Orlando, FL; 2005.
- [7] Doney R, Sen S. Ordered and highly scalably granular media for shock mitigation. US Army Research Laboratory, ARL-TR-3612; 2005.
- [8] Fink BK. Performance metrics for composite integral armor. US Army Research Laboratory, ARL-RP-8; 2000.
- [9] Dharmasena KP, Wadley HNG, Xue A, Hutchinson JW. Mechanical response of metallic honeycomb sandwich panel structures to highly-intensity dynamic loading. *Int J Impact Eng* 2008;35:1063–74.
- [10] Brutcher RL, Morse DE. Temperature-free, low-temperature synthesis of crystalline barium titanate nanoparticles under bio-inspired conditions. *Angew Chem Int Ed* 2006;45:6564–6.
- [11] Fantner GE, Rabinovich O, Schitter G, Thurner P, Kindt JH, Finch MM, et al. Hierarchical interconnections in the nano-composite material bone: fibrillar cross-links resist fracture on several length scales. *Compos Sci Technol* 2006;66:1202–8.
- [12] Huang J, Venkataraman S, Haftka RT, Rapoff AJ. Design for stress concentrations near holes via biomimetics. Final Report – NASA SBIR Phase 2 Contract #99-2-05.04-9943; 2003.
- [13] Martin RB. Determinants of the mechanical properties of bones. *J Biomech* 1991;24(S1):79–88.
- [14] Martin RB, Burr DB, Sharkey NA. *Skeletal tissue mechanics*. Springer; 1998.
- [15] Huang J, Rapoff AJ, Haftka RT. Attracting cracks for arrestment in bone-like composites. *Mater Des* 2006;27(6):461–9.
- [16] Ashby MF, Evans A, Fleck NA, Gibson LJ, Hutchinson JW, Wadley HHG. *Metal foams: a design guide*. Heinemann: Butterworth; 2000.
- [17] Gama BA, Bogetti TA, Fink BK, Yu CJ, Claar TD, Eifert HH, et al. Aluminum foam integral armor: a new dimension in armor design. *Compos Struct* 2001;52:381–95.
- [18] Chowdhury MR, Tabiei A. Air gun launch simulation modeling and finite element model sensitivity analysis. US Army Research Laboratory, ARL-TR-3703; 2006.
- [19] Kelly R, Richman G. *Principles and techniques of shock data analysis, SVM-5. The Shock and Vibration Information Center, United States Department of Defense*, Washington, DC; 1969.